CRREL

CRREL REPORT 92-12

Shock Response of Snow
Analysis of Experimental Methods and Constitutive Model Development

Jerome B. Johnson, Jay A. Brown, Edward S. Gaffney,
George L. Blaisdell and Daniel J. Solie

July 1992

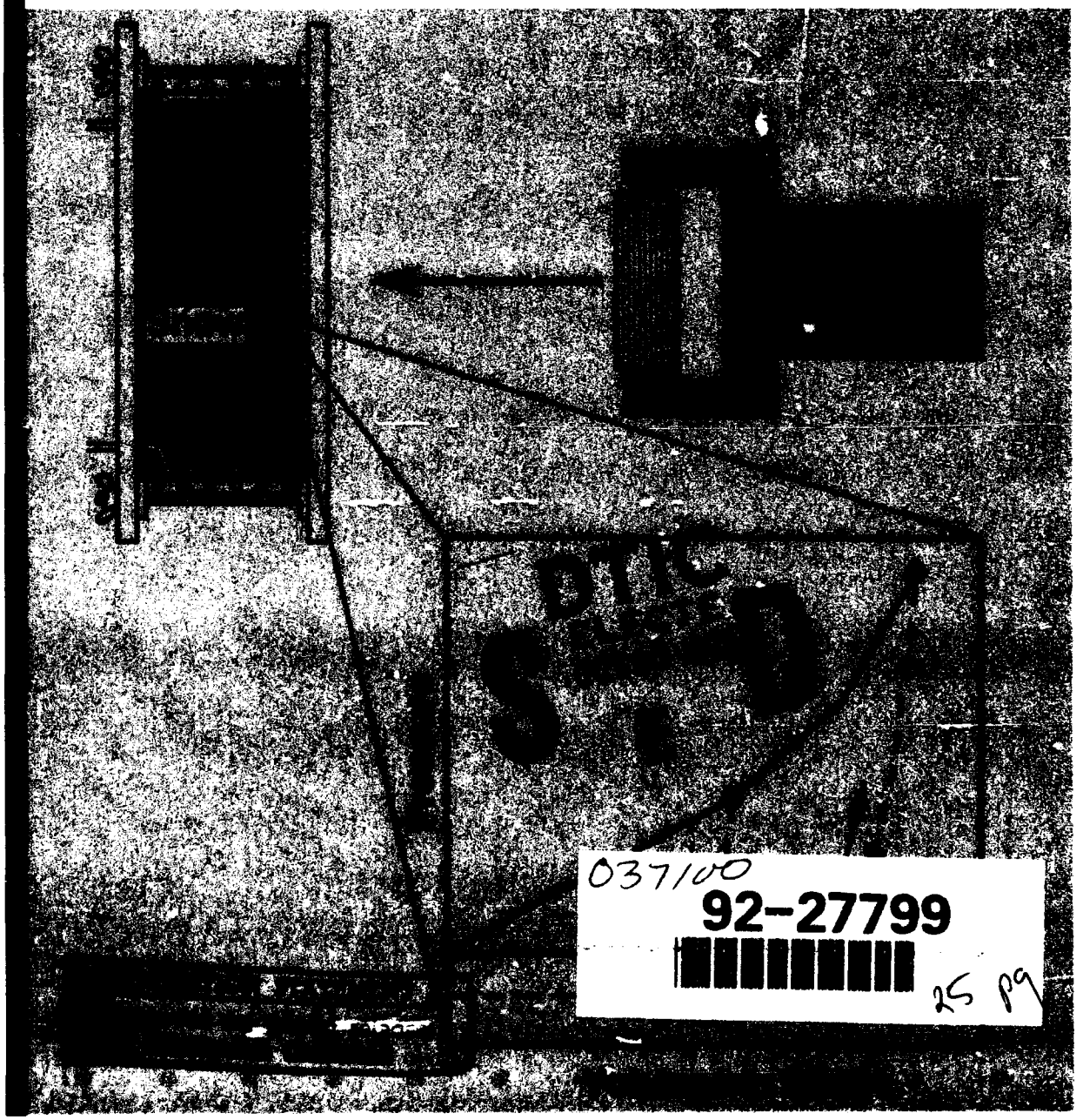

For conversion of SI metric units to U.S./British customary units of measurement consult ASTM Standard E380, Metric Practice Guide, *published by the American Society for Testing and Materials, 1916 Race St., Philadelphia, Pa. 19103.*

COVER: Schematic of the experimental apparatus and the P-V curve.

CRREL Report 92-12

U.S. Army Corps
of Engineers
Cold Regions Research &
Engineering Laboratory

Shock Response of Snow

Analysis of Experimental Methods and Constitutive Model Development

Jerome B. Johnson, Jay A. Brown, Edward S. Gaffney,
George L. Blaisdell and Daniel J. Solie

July 1992

Prepared for
OFFICE OF THE CHIEF OF ENGINEERS

PREFACE

This report was prepared by Dr. Jerome B. Johnson, Geophysicist, Applied Research Branch, Experimental Engineering Division, U.S. Army Cold Regions Research and Engineering Laboratory (CRREL); Dr. Jay A. Brown, Physicist, Los Alamos National Laboratory; Dr. Edward S. Gaffney, Geologist, Ktech Corporation; George L. Blaisdell, Research Civil Engineer, Applied Research Branch, Experimental Engineering Division, CRREL; and Dr. Daniel J. Solie, Physical Scientist, Applied Research Branch, Experimental Engineering Division, CRREL. The research described in this report was funded by DA Project 4A762784AT42, *Cold Regions Engineering Technology*; Work Unit CS/012, *Attenuation of Shock Waves by Snow.*

Dr. T. Day, Los Alamos National Laboratory, technically reviewed this report.

The contents of this report are not to be used for advertising or promotional purposes. Citation of brand names does not constitute an official endorsement or approval of the use of such commercial products.

CONTENTS

ILLUSTRATIONS

Figure

TABLES

Table

Shock Response of Snow

Analysis of Experimental Methods and Constitutive Model Development

JEROME B. JOHNSON, JAY A. BROWN, EDWARD S. GAFFNEY,
GEORGE L. BLAISDELL AND DANIEL J. SOLIE

INTRODUCTION

A constitutive model of the shock compression of snow is of interest for its direct application to such fields as planetary sciences, cold regions and military engineering, and shock isolation. The only existing data obtained with reliable experimental methods are the high-pressure data (3.8–35.4 GPa) of Bakanova et al. (1975). Experiments by Napadensky (1964), Wakahama and Sato (1977), Sato and Brown (1983) and Sato (1987) did not meet criteria for steady plane-wave propagation even though the data were reduced using that assumption.

We have conducted a test program using embedded stress gauges to obtain stress–strain relations for snow (Brown et al. 1988). The unsteady nature of shock wave propagation in the snow, the specialized sample preparation methods, and the large impedance mismatches between the snow and stress gauges resulted in complex stress histories. These features precluded direct application of the Rankine–Hugoniot jump conditions or the Lagrangian conservation equations for mass, momentum and energy (Fowles and Williams 1970, Seaman 1976) to analyze the experimental results. Instead, a detailed analysis of one of our experiments, using the PRONTO 2D dynamic finite-element program (Taylor and Flanagan 1987), was conducted to determine the origins of distinctive features from measured stress histories and to determine loading, unloading and reloading paths for the snow. In this paper we discuss our experimental procedures and difficulties, the data records for a typical shot, our assumptions for determining the initial loading curve, and unloading and reloading curves for the snow, as well as our results. The overall shock response of snow derived from the entire shot test series will be presented separately.

EXPERIMENTAL METHODS

A shock wave experiment was conducted using a 200-mm-diameter gas gun to obtain uniaxial strain loading in snow. A flat-faced 35.9-mm-thick, polymethyl methacrylate (PMMA) flyer plate was accelerated with compressed nitrogen gas to impact a snow target.

The target assembly consisted of a copper cylinder with sealed aluminum capping end plates to provide a vacuum-tight cannister (Fig. 1). A vacuum-tight target assembly was required because the target chamber of the gas gun was evacuated prior to firing. The snow, which had a vapor pressure of about 300 Pa, would have sublimated if it had not been isolated in a sealed cannister. A spiral of copper tubing was soldered around the copper cylinder, allowing refrigeration of the sample once the target had been mounted on the gas gun. The target was assembled in an adjacent coldroom with the target axis vertical. A buffer plate, consisting of a carbon stress gauge epoxied between two aluminum plates (12.7-mm-thick plate epoxied to a 6.4-mm-thick plate), formed the front of the target.

Snow was sieved into the copper cylinder in stages, with stress gauges clamped in place at specific distances from the aluminum/snow interface (Table 1). The stress gauges were placed off-axis so that the shock wave had a direct, unobstructed path from the buffer through the snow to each gauge. Our snow had approximately millimeter-sized grains. Consequently our uncertainty of gauge position was about ±1 mm, which for this experiment corresponds to an uncertainty in arrival time of about ±5 μs.

Thermocouples were placed in the snow and were used to monitor the sample temperature. The copper cylinder was completely filled with snow, and the instrumentation wires were run along the inside wall of

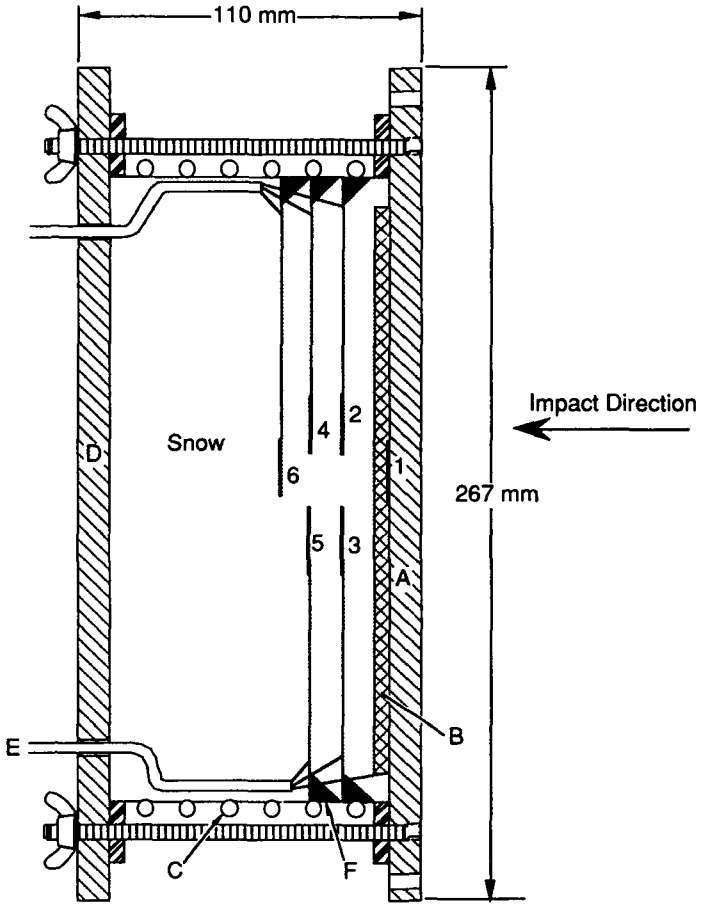

Figure 1. Schematic of the snow target assembly, consisting of an aluminum plate (A and B), a carbon gauge (1), a cooling coil (C) soldered to a copper cylinder, an aluminum back support plate (D), gauge and thermocouple leads exiting the rear surface (E), and a gauge support pedestal mounted to the inside wall of a copper cylinder (F).

the copper cylinder and through vacuum-sealed holes in the back plate (12.7-mm aluminum). Six shorting pins, each with a different length, were mounted concentrically on the outer edge of the aluminum. These shorting pins were used to determine the flyer plate impact velocity and to trigger data acquisition.

After the target was assembled, the sample was "cold soaked" in a refrigerated room overnight before being mounted on the end of the gas-gun barrel. Snow temperature was controlled by circulating cold nitrogen gas through the copper tubing attached to the outer wall of the target.

Stress–time records were measured using 50-ohm carbon-film piezoresistive gauges (Krehl 1978). Their high sensitivity allows for a relatively low excitation power and less Joule heating of the gauge compared to other piezoresistive gauges. The gauge has a calibration uncertainty on loading and unloading of between 5 and

Table 1. Stress gauge positions relative to the snow/aluminum interface.

Gauge plane	*Gauge number*	*Relative position (mm)*	*Gauge thickness (mm)*	*Average relative position (mm)*
0	1	–6.45 ± 0.01	0.1778*	–6.45
1	2	13.2 ± 1	0.8128	14.0
	3	14.8 ± 1	0.6604	
2	4	27.2 ± 1	0.6858	26.0
	5	24.8 ± 1	0.5080	
3	6	37.2 ± 1	0.5824	37.2

*Includes epoxy and mylar tape (the unclad thickness was 0.0762 mm).

10% of the stress at stresses below about 2.0 GPa (Gourdin and Weinland 1986, King and Janée 1987). Hysteresis effects range from 0 to 9% of the stress on partial or complete unloading (King and Janée 1987). Our experience in using the gauge in soils and aluminum have not shown evidence of measurable hysteresis. The active element for the carbon gauge (0.75 × 1.25 cm) forms a single, continuous, wide strip rather than a grid, as is the case for the more commonly used manganin and ytterbium gauges; it is thus less susceptible to puncturing by individual snow grains. The gauges were encapsulated between 0.025-mm-thick layers of kapton. Recording life was extended by using a 0.19- to 0.34-mm layer of mica as armor.

Pulsed Wheatstone bridge power supplies were used to provide 70 V of gauge excitation for 200 μs. Bridge output signals were recorded digitally using CAMAC-based waveform digitizers with a band width of 1 MHz and a sampling rate of 2 MHz.

EXPERIMENTAL RESULTS AND DIFFICULTIES

Figure 2 shows data from the six stress gauges in the target assembly (Fig. 1): one in the aluminum buffer and the remainder in the snow (compressive stresses are treated as positive). For this shot the snow had an initial density of 400 kg m^{-3} and a temperature of –8°C. The flyer plate impact velocity was 150.7 m s^{-1}, resulting in about a 0.4-GPa peak impact stress with four reverberations in the target buffer (Fig. 2, gauge 1 at gauge plane

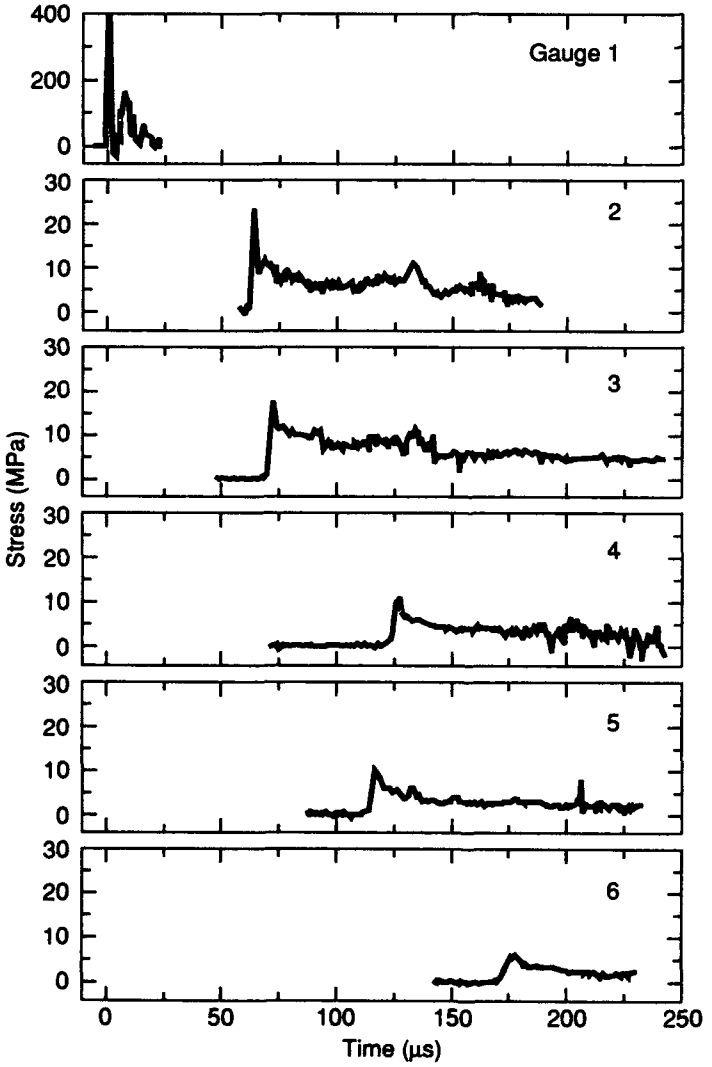

Figure 2. Stress records from gauge 1 in the aluminum and gauges 2–6 embedded in snow.

0). Shock propagation velocities in the snow were 242 ± 15 m s^{-1} at gauge plane 1 (gauges 2 and 3), 230 ± 15 m s^{-1} at gauge plane 2 (gauges 4 and 5) and 205 ± 15 m s^{-1} at gauge plane 3 (gauge 6). Gauge records from the first gauge plane show an initial spike at shock arrival, a gradual decrease to a minimum value of about 7–8 MPa followed by a shallow rise to about 8–10 MPa. A slight dip in stress level then occurs, with a spike at 135 μs before a decrease in stress below 7 MPa. The stress records at the second and third gauge planes show a significantly longer initial rise time and smaller spikes. Rankine–Hugoniot theory predicts a stress level of about 12 MPa for a steady wave traveling at 240 m s^{-1} in the snow if the snow particle velocity was equal to the maximum possible buffer particle velocity after impact with the PMMA flyer plate (about 120 m s^{-1}).

The generally good agreement, within experimental uncertainty, between the stress records in the same plane for gauges 2 and 3, and gauges 4 and 5, and the fact that pseudo-steady stresses for gauges 2 and 3 are on the same order as estimated using Rankine–Hugoniot theory, suggest that the measured records are valid.

The stress records from all of the gauges in the snow are both complex and unsteady. Two factors—target design and impedance mismatching between the snow and stress gauges—contribute to the complexity. Our target design was constrained by the need for a vacuum-tight container that would still produce a one-dimensional strain shock when impacted. We achieved a flat impact surface by using a thick buffer of sufficient strength to prevent any significant deflections due to the pressure difference between the interior of the target and the target chamber. Upon impact from the flyer plate, the buffer imparted stresses to the snow, which gradually decreased as the momentum was transferred from the buffer to the target by multiple reverberations in the buffer. The rate of decrease in applied stress was controlled by the impedance mismatch between the buffer and the snow. A large impedance mismatch between the stress gauges and the snow produced large-amplitude reflected pulses, further complicating the signal (Brown et al. 1988, Gaffney 1989). Shock wave stress records were sufficiently long that waves generated at the edge of the target propagated to the stress gauges prior to the end of the experiment.

MODEL SIMULATION OF THE EXPERIMENTAL DESIGN

We used the PRONTO 2D transient solid dynamics finite-element program as a tool to understand the complex wave records and to construct constitutive models of shock propagation in snow. We initially constructed a simple model incorporating only the flyer, buffer and snow in a one-dimensional (1D) geometry. Ultimately it was necessary to include the stress gauges and the failure strength of the epoxy bond between the two plates that made up the buffer in the 1D model. Figure 3 shows the final model geometry used in our 1D analysis. In the model a PMMA flyer impacted an aluminum buffer that had a no-friction contact with the snow. The aluminum buffer, in the model, consisted of a mylar layer sandwiched between two plates of aluminum tooling plate, which simulated the epoxy, mylar tape and stress gauge between the two buffer plates used in the test experiment. Mica-clad gauges were simulated by layers of mica at the average position of gauges 2 and 3 for the first gauge plane and gauges 3 and 4 for the second gauge plane. The third gauge plane was placed at the same position in the finite-element mesh as the gauge 6 position in the actual test. Gauge dimensions used in the model were taken from gauges 2, 4 and 6 (Table 1).

The PMMA and aluminum were modeled as an elastic–plastic–hydrodynamic material. This model combines a Von Mises yield condition including strain hardening to describe the deviatoric response. Volumetric response is represented by a Mie–Gruneisen equation of state (EOS) of the form

$$P = k_0 \eta \left(1 + k_1 \eta + k_2 \eta^2 \right) \left(1 - \frac{\Gamma_0 \eta}{2} \right) + \frac{\Gamma_0 \rho_0}{\rho} E_v \qquad (1)$$

where

E_v = energy per unit volume
ρ_0 = initial density
ρ = density at pressure P
η = $(1 - \rho_0 / \rho)$

and the remaining parameters are material-dependent properties and are given in Table 2. Mylar was modeled as a pure hydrodynamic material using the EOS parameters tabulated. Mica was treated as an elastic material. Although both deviatoric behavior and volumetric behavior of the materials were included in the model, changes in deviatoric parameters had a negligible effect on the calculated results.

Modulation of the uniaxial strain conditions in our impact experiment by release waves, generated at the lateral edge of the target, was examined using an axisymmetric two-dimensional (2D) model (Appendix A). Material parameters and the constitutive model for snow were the same for both the 2D and 1D models.

In constructing our model we used the measured stresses as a guide to establish the validity of calculated results. The measured stress–time record for gauge 1 (Fig. 2) was used to determine if the calculated stresses

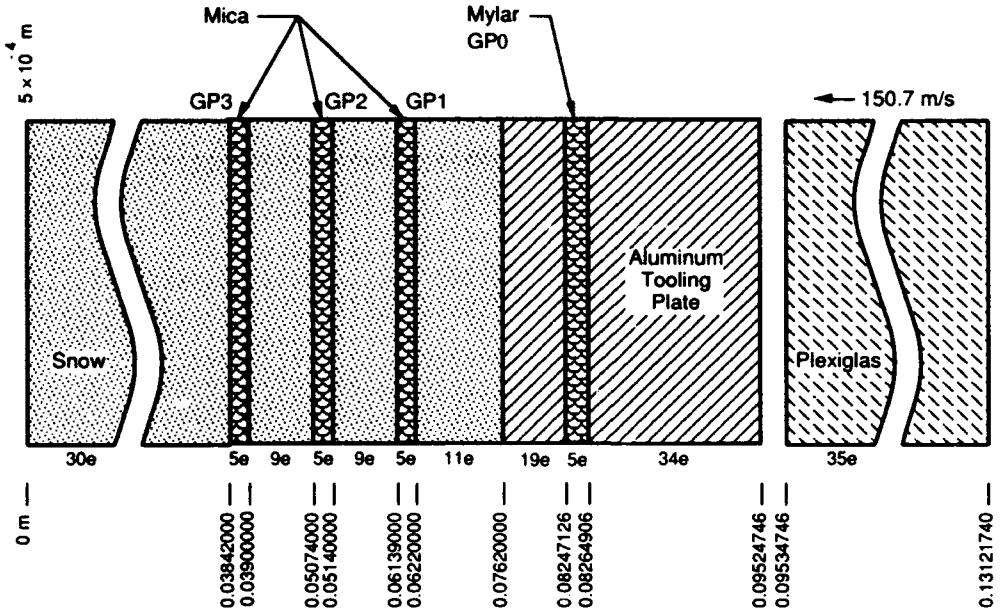

Figure 3. Schematic of the experimental configuration used to generate the one-dimensional finite-element mesh for PRONTO 2D. Gauge planes 0, 1, 2 and 3 are designated by GP0, GP1, GP2 and GP3 in the figure. The mesh was one element wide, with the number of lateral elements for each component shown in the figure.

from the model produced by the impact of the PMMA flyer and aluminum buffer were realistic. Figure 4 shows a comparison of the model-calculated stresses in the buffer, at the location of gauge 1, and the measured stresses determined from gauge 1. Calculated stresses in the buffer were not significantly influenced by the snow behavior for any reasonable choice of snow pressure vs volumetric strain (P–V) curve. The calculated and measured stresses agree very well for the first peak and fall. Thereafter there is fair agreement in the timing of the respective maxima and minima. The four reverberations calculated by the model are caused by reflected waves from the aluminum/snow interface and the PMMA/aluminum interface. The reverberations end when the unloading wave from the back of the PMMA flyer arrives at the mylar layer, causing

Table 2. Constitutive model parameters used to develop the PRONTO 2D model calculation.

Material	*Model type*	*Density* ($kg\ m^{-3}$)	*Young's modulus* (GPa)	*Poisson's ratio*	*Yield strength* (MPa)	*Hardening modulus* (MPa)	*Beta*	*Pressure cutoff* (MPa)	k_0 (GPa)	k_1	k_2	G_0
PMMA*	Elastic/plastic-hydrodynamic	1184	6.3	0.4	375	500	0.5	−100	5.83	4.42	13.04	0.7
Aluminum†	Elastic/plastic-hydrodynamic	2828	72.5	0.33	270	1150	0.5	−1000	81.86	2.81	7.25	2
Mylar**	Hydrodynamic	1390							6.73	1.196	2.29	1
Mica††	Elastic	2844	69.6	0.26								

*PMMA EOS data (Rice 1980) were reformulated to conform to the PRONTO 2D representation of the Mie-Gruneisen EOS, and the hardening modulus was estimated. Beta is a parameter that determines the amount of isotropic and kinematic hardening and was estimated.

†Aluminum EOS from Rice (1980). The hardening modulus was determined from data given by Herrmann and Lawrence (1978). Beta was estimated.

**Mylar EOS from Louie et al. (1970).

††Calculated from isotropic elastic moduli (Vaughan and Guggenheim 1986).

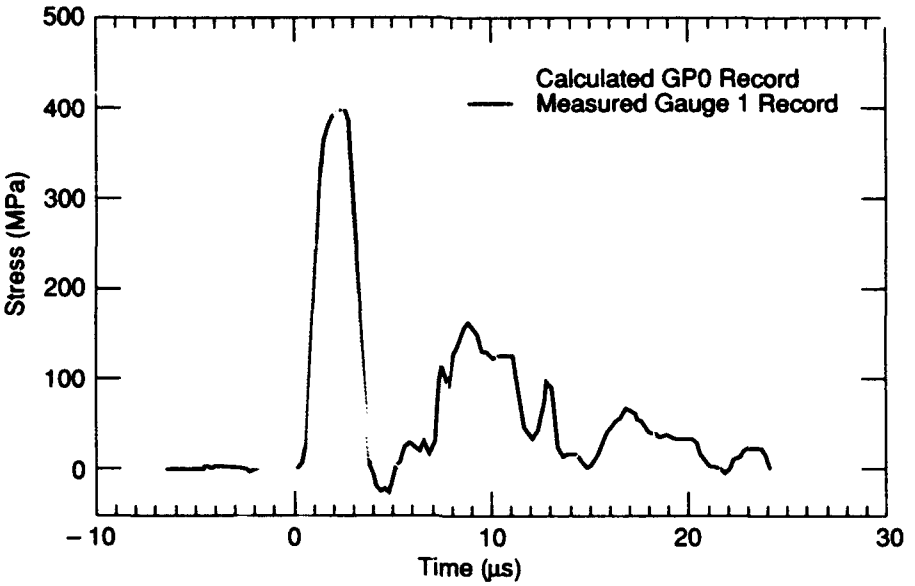

Figure 4. Comparison of the calculated stresses for gauge plane 0 with the measured stress record for gauge 1, located in the aluminum buffer.

debonding. Calculations have shown that tensile stresses in the buffer would have exceeded 120 MPa had the band between the mylar and the aluminum not been allowed to fail. The reduction in calculated peak stress for each succeeding reverberation is controlled by the impedance mismatches at the aluminum/PMMA flyer interface and the aluminum/snow interface. The most probable explanation for the difference between measured and calculated stresses for the later reverberations is that gauge 1 and/or the epoxy/mylar bond was damaged after being subjected to a tensile stress of about 25 MPa at 4.8 μs (Fig. 4). Also the carbon gauges are not designed to measure tensile stresses. Epoxy resins, such as we used in manufacturing the buffer, have tensile strengths that range from 14 to 90 MPa, depending on their composition (Baumeister and Marks 1967). After the first tensile pulse the gauge was still able to sense compressive stresses but not tensile stresses. The gauge failed completely upon the arrival of the unloading wave from the flyer (Fig. 4). This unloading wave also caused the two parts of the buffer plate to separate. The low-amplitude stresses (less than 10 MPa) in the calculated record after the arrival of the unloading wave, shown in Figure 4, are caused by reverberations in buffer disk B (in contact with the snow, Fig. 1). These reverberations cause the gradual decrease in stresses in the snow after shock front passage.

Measured stress–time records from gauges embedded in the snow were used to aid in our construction of a constitutive relationship for snow compaction. This was accomplished by assuming that snow strain-hardens during all stages of its compaction and that the form of the dynamic P–V curve is similar to that found from quasi-static uniaxial strain tests (Abele and Gow 1975). That is, the slope of the stress–strain curve is either increasing or constant with increasing volumetric strain.

We used the Soils and Crushable Foams material model in PRONTO 2D to describe snow compaction. This phenomenological model was constructed from a version of the model developed by Krieg (1978) and described by Swenson and Taylor (1983). It consists of a yield function describing deviatoric deformations uncoupled from the P–V curve used to define volumetric deformations. The yield surface σ_y is a surface of revolution about the hydrostat specified as a quadratic in pressure

$$\sigma_y = a_0 + a_1 P + a_2 P^2 . \qquad (2)$$

We used $a_0 = 10$ kPa, $a_1 = 0.1$ and $a_2 = 0.0$ in our calculations. The choice of parameters in the yield function does not greatly affect the results since the deformations are dominated by volumetric compaction. Allowing the yield function to depend slightly on pressure does, however, greatly increase the stability of the calculation.

The user-defined function $f_P(\varepsilon_v^{max})$, where the volumetric strain is $\varepsilon_v = -\ln(\rho_0/\rho)$, is used to define the P–V curve (Taylor and Flanagan 1987). This function incorporates both a loading curve and a linear unloading–reloading curve. The slope of the unloading curve

is required to be greater than the loading P–V curve. The function

$$\phi_P = P - f_P(\varepsilon_v^{max}) \quad (3)$$

where ε_v^{max} is the maximum ε_v experienced by each element, defines the motion of the end cap of the deviatoric yield function along the hydrostat. Tensile failure is assumed to occur if the pressure is less than a user-defined fracture pressure P_{fr}. Tensile failure strain ε_{fr} is initially negative and is set to P_{fr}/K_0, where K_0 is the initial bulk modulus of the snow; ε_{fr} increases with ε_v^{max} and is determined by unloading from the $f_P(\varepsilon_v^{max})$ curve along a linear unloading–reloading curve to P_{fr}. The strain at P_{fr} is the new value of ε_{fr}.

The results of preliminary calculations using the Soils and Crushable Foams model replicated many features of our measured data, including arrival times and peak stresses that are in good agreement with measurements (Johnson et al. 1990). However, the post-peak stress histories could not be reproduced because of the restrictions that the unloading–reloading curve be linear, have the same value as the initial bulk modulus irrespective of the total volumetric strain, and have a slope greater than the maximum slope of the P–V curve. We modified the Soils and Crushable Foams model to accommodate more general unloading and reloading behavior for snow. On initial loading, the pressure in the snow is a function of ε_v^{max}, as was the case in the original model. Multiple linear or nonlinear unloading paths may be defined, with each unloading path being defined over a specified range of ε_v. One of two possible reloading schemes may be used: reloading along the same path as unloading or reloading along a chord from the last P–V state to the $f_P(\varepsilon_v^{max})$, ε_v^{max} state (Appendix B).

CONSTITUTIVE RELATIONSHIP AND DISCUSSION

Development of a constitutive relationship proceeded in two stages by first finding a P–V curve that produced a good agreement between calculated and measured shock arrival times. Next, the stress history after shock arrival was used to constrain the unloading and reloading curves. The P–V curve and the unloading and reloading curves found by comparing calculated and measured results are not unique. They can vary because of experimental uncertainties, the complex relationship of one segment of the P–V curve to another, and the subjective determination of what constitutes a good model simulation of the measured results.

The range of possible P–V curve shapes was constrained in this study by several factors. We assumed that the slope of the P–V curve either increases or remains constant with increasing volumetric strain (which is consistent with observations from quasi-static tests on snow assuming no phase changes occur). We have included the further constraint that the final density for the snow must be less than that of our recovered post-experiment samples (860 kg m^{-3}). In addition, our calculations have shown that the P–V curve can be broken into two regions, which affect the shock wave differently. The magnitude of the P–V curve in the mid-stress range (2.5 MPa $\leq P \leq$ 16 MPa) affects the shock velocity and produces moderate changes in the magnitude of post-peak stresses. The magnitude of the P–V curve in the high-stress range (16 MPa $\leq P \leq$ 40 MPa) does not affect shock velocity but is important in reproducing the shock arrival stress spikes at the stress gauges and does affect the post-peak stress amplitudes. The P–V curve definition in the low-stress range could not be determined directly from our tests. The curves were estimated from the quasi-static test results of Abele and Gow (1975). Unloading and reloading curves were constrained by the shock wave arrival times and stress magnitudes of waves reflected from gauges in the snow and from the aluminum/snow interface. The unloading and reloading curves were further constrained by comparing the attenuation of the calculated peak stresses and the magnitude and frequency of post-peak stress oscillations with those measured.

Initial calculations used a P–V curve from a quasi-static compaction test by Abele and Gow (1975) (Table 3). These produced arrival times that were much later than measured for all gauges in the snow. Succeeding calculations were made after increasing the model P–V curve slope in a systematic manner (that is, increasing the stress needed to cause a given volumetric strain). The final P–V curve and the unloading curves used to calculate the results presented in this paper are shown in Figure 5 and listed in Table 4. The calculated peak stresses for gauges 2, 3, 4 and 5 and the post-peak stress history for gauge 1 agree with measured values within the limits of experimental error. The calculated stresses for gauge 6 are larger than for the measured record but have the same form. Differences between the calculated stress histories for gauges 4, 5 and 6 and the measured values may result from superposition of release waves that originated at the edge of the aluminum, degrading the uniaxial strain conditions.

Comparison of the 1D calculated and measured stresses for gauges 2 and 3 are shown in Figure 6. This provides a means of identifying important processes affecting the shock propagation. Calculations show that impedance mismatch between the gauges and the snow produced the stress spike at shock arrival. The measured

Table 3. *P-V* curve parameters for Abele and Gow's measurements (1975).

$f_p(\varepsilon_v^{max})$ (MPa)	Density ($kg\ m^{-3}$)	ε_v	2μ (MPa)	K_0 (MPa)	P_{fr} (MPa)
0.0	390	0.0	710*	200†	–0.01
0.07	435	0.109			
0.14	461	0.167			
0.28	570	0.379			
0.7	581	0.399			
1.4	649	0.509			
2.1	680	0.556			
2.88	719	0.612			

*The shear modulus μ was estimated from acoustic data on snow.
†The initial bulk modulus K_0 was chosen to be about the same as the bulk modulus of ice.

stress after shock arrival decreases to that of the ambient snow stress. Measured stresses then increase at 95 μs and remain elevated until about 120 μs. Calculations indicate that the stress rise from 95 to 120 μs is due to a shock pulse that had been reflected from gauge plane 1 propagated back to the aluminum/snow interface and reflected back to gauge plane 1. The doubly reflected wave shows the effects of dispersion and attenuation during its travel. At 120 μs the measured stress begins to decrease because of unloading from the buffer. The measured stress decrease is interrupted by the arrival of a shock pulse that calculations indicate originated from a reflected wave at the second gauge plane (the gauge located at 0.0514 m in Fig. 3, gauge plane 2). This produces a sharp stress rise at 135 μs, then a stress decrease to the stress magnitude of the buffer unloading wave.

Calculations using the 2D model (Appendix A) show that gauge plane 1 stresses are not significantly affected by release waves originating at the edge of the

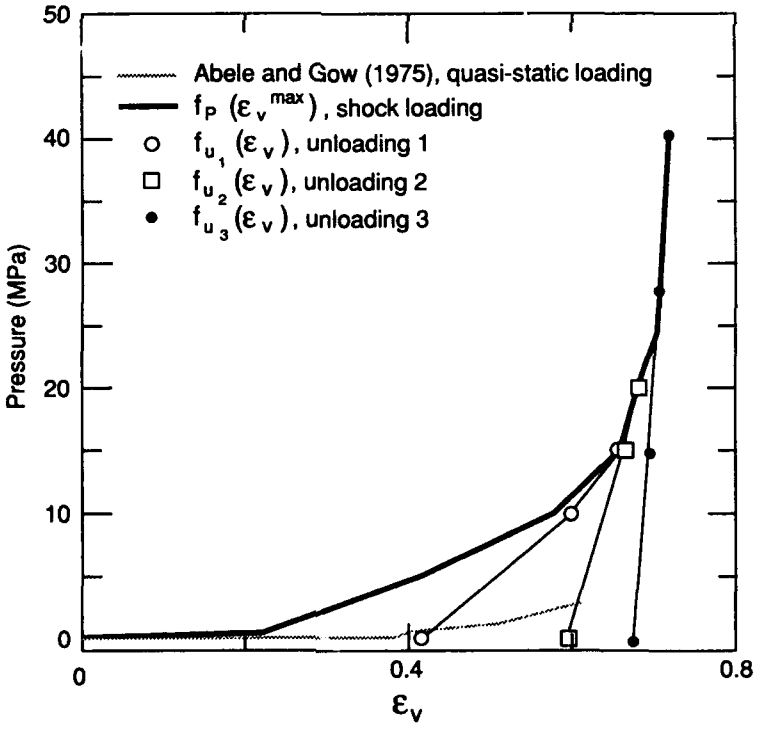

Figure 5. Loading pressure–volumetric strain curve and unloading–reloading curves used in PRONTO 2D to model snow compression and Abele and Gow's quasi-static pressure–volumetric strain results.

Table 4. Snow *P-V* curve parameters, moduli data and unloading curve parameters used to define snow behavior in PRONTO 2D model calculations.

$f_p(\varepsilon_v^{max})$			$f_{\mu 1}(\varepsilon_v)$			$f_{\mu 2}(\varepsilon_v)$			$f_{\mu 3}(\varepsilon_v)$					
Density ($kg\ m^{-3}$)	P_k *(MPa)*	ε_{vk}	P_{1m} *(MPa)*	K_{1m} *(MPa)*	$\varepsilon_{\mu 1}$	P_{2m} *(MPa)*	K_{2m} *(MPa)*	$\varepsilon_{\mu 2}$	P_{3m} *(MPa)*	K_{3m} *(MPa)*	$\varepsilon_{\mu 3}$	2μ *(MPa)*	K_0 *(MPa)*	P_{fr} *(MPa)*
400	0	0.0	10	55	0.681	15	217	0.718	15	800	0.764	710	4.2	–0.01
550	0.35	0.318	15	80		20	265		30	835				
635	5.0	0.462							40	2700				
740	10.0	0.615												
790	15.0	0.681												
820	20.0	0.718												
840	25.0	0.742												
848	30.0	0.751												
859	40.0	0.764												

aluminum until about 30 μs after the peak stress arrival. Stresses are reduced for the following 25 μs, then increase to slightly larger magnitudes than expected for 1D wave propagation. This is consistent with the measured stresses for gauges 2 and 3, which show pronounced stress reductions about 20 μs after peak stress arrival. Stresses increase again 20–30 μs later, just prior to the arrival of the reflected pulse from gauge plane 2. We cannot unambiguously interpret the measured stress rise for gauges 2 and 3 at about 110 μs since 1D model calculations indicate that reflected waves from the aluminum/snow interface arrive at between 95 and 120 μs, overlapping the arrival of the 2D release waves.

Figure 7 compares the calculated stress history for gauge plane 2 with measured stresses from gauges 4 and 5. The peak calculated stress is about the same as was measured. The 2D analysis indicates that release waves begin affecting the shock wave upon arrival at gauge plane 2. Differences between the post-peak calculated and measured stresses are attributed to release wave superposition on the 1D stresses.

Calculated stresses for gauge plane 3 have the same form but larger amplitude than the stresses measured by gauge 6 (Fig. 8). Analysis using the 2D model indicates that release waves propagating from the aluminum buffer reduce stress magnitudes at gauge plane 6 but do

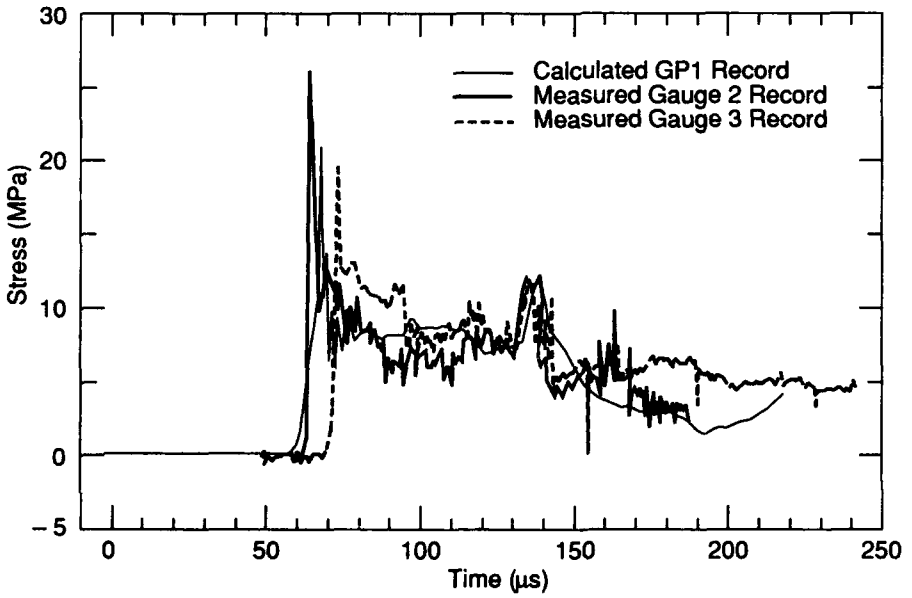

Figure 6. Comparison of the calculated stresses for gauge plane 1 with measured stress records for gauges 2 and 3.

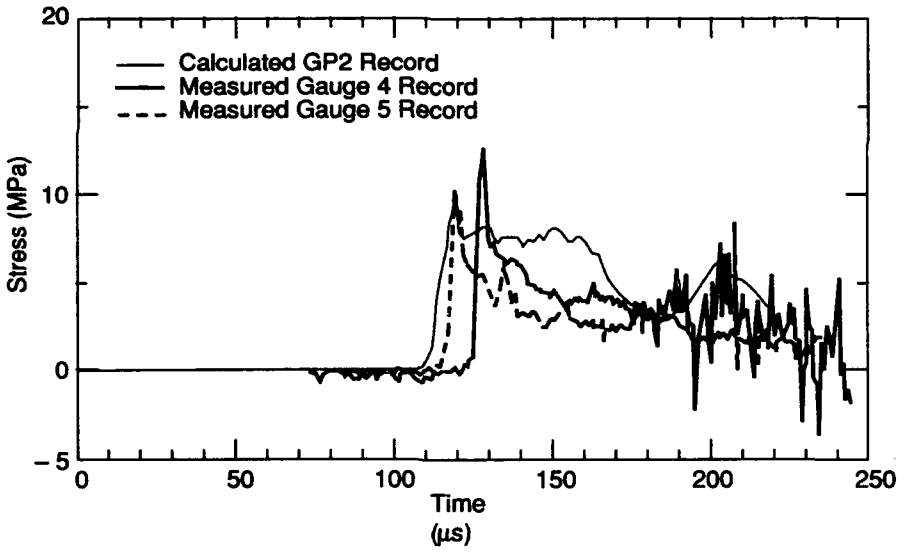

Figure 7. Comparison of the calculated stresses for gauge plane 2 with measured stress records for gauges 4 and 5.

not affect the wave form significantly. This suggests that magnitude differences between measurements and calculations are caused by the 2D edge effects.

CONCLUSION

The complex unsteady stress histories from a uniaxial strain impact on snow have been simulated using the PRONTO 2D transient solid dynamics finite-element program.

The *P–V* curve estimated using PRONTO 2D is not unique and can vary because of experimental uncertainties, the interdependent influences of different regions of the curve, and the subjective determination of what constitutes a good model simulation. The range of possible *P–V* curve shapes is constrained by separate physical properties in two of the major stress regions. The mid-stress range of the curve is determined by shock velocity and pseudo-steady stress levels. The high-stress region of the curve is constrained by the magnitudes of stress spikes at the gauges. The low-stress region is estimated from the quasi-static results of Abele and Gow (1975).The shape of the *P–V* curve

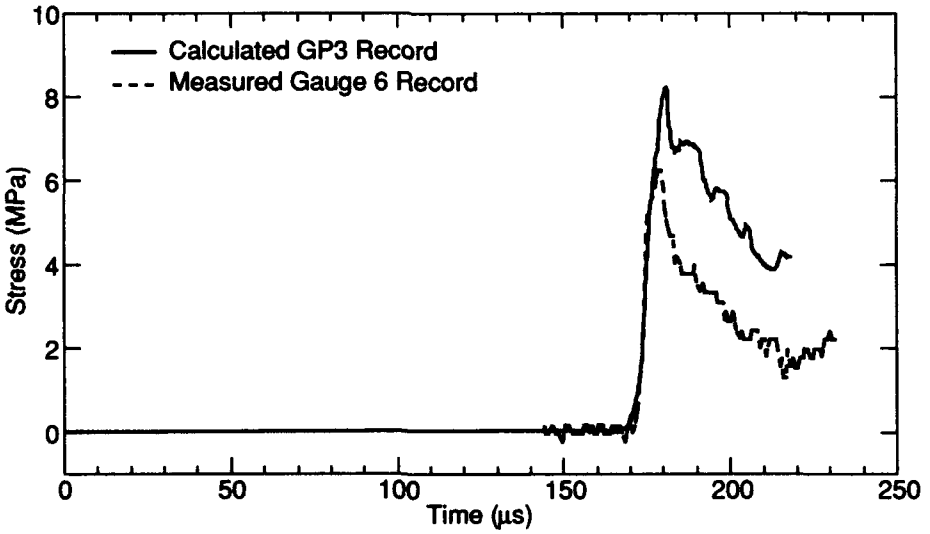

Figure 8. Comparison of the calculated stresses for gauge plane 3 with measured stress records for gauge 6.

is further constrained by the assumptions that slope either increases or remains constant with increasing volumetric strain and that the final density for the snow must be less than 860 kg m^{-3}. Calculations have shown that slight variations in *P–V* curve shape do not significantly change the calculated stress histories. Abele and Gow's (1975) quasi-static *P–V* curve lies well below the range consistent with the shock data, implying a strong strain-rate dependence for shock wave deformation in snow. Post-peak stresses are strongly controlled by the unloading and reloading behavior of the snow. The unloading curve for snow is a nonlinear function of volumetric strain. Reloading is along a chord from the last *P–V* state to the maximum pressure [$f_P(\varepsilon_V^{max})$] and maximum volumetric strain (ε_V^{max}) state (Fig. B1) producing a hysteretic unloading–reloading cycle that is consistent with quasi-static unloading and reloading in other porous media (Johnson and Green 1976, Larson and Anderson 1979).

LITERATURE CITED

Abele, G. and A. J. Gow (1975) Compressibility characteristics of undisturbed snow. USA Cold Regions Research and Engineering Laboratory, Research Report 336.

Bakanova, A.A., V.N. Zubarev, Yu.N. Sutulov and R.F. Trunin (1975) Thermodynamic properties of water at high temperatures and pressures. Sov. Phys.-JETP, vol. 41, p. 544–548. (Originally published as Zh. Eksp. Teor. Fiz., vol. 68, p. 1099–1107).

Baumeister, T. and L.S. Marks (Ed.) (1967) *Standard Handbook for Mechanical Engineers*. Seventh ed. New York: McGraw-Hill.

Brown, J.A., E.S. Gaffney, G.L. Blaisdell and J.B. Johnson (1988) Techniques for gas gun studies of shock wave attenuation in snow. In *Shock Waves in Condensed Matter 1987, Proceedings of the American Physical Society Topical Conference on Shock Waves in Condensed Matter, 20–24 July, Monterey, California* (S.C. Schmidt and N.C. Holmes, Ed.). Elsevier Science Publishers, p. 657–660.

Fowles, R. and R.F. Williams (1970) Plane stress wave propagation in solids. *Journal of Applied Physics*, **41:** 360–363.

Gaffney, E.S. (1989) Numerical models of shock waves in snow. Ktech Corporation, TR 89–03 (Final Report to CRREL under contract DACA8988M0734).

Gourdin, W.H. and S.L. Weinland (1986) Performance of piezoresistive carbon sensors in contact with porous materials. *Review of Scientific Instruments*, **57:** 1422–1426.

Herrmann, W. and R.J. Lawrence (1978) The effect of material constitutive models on stress wave propagation calculations. *ASME Transactions, Journal of Engineering Materials and Technology*, **100:** 84–95.

Johnson, J.B., J.A. Brown and E.S. Gaffney (1990) Interpretation of the stress histories from shock impact tests on snow using embedded stress gauges. In *Shock Compression of Condensed Matter 1989, Proceedings of the American Physical Society Topical Conference on Shock Compression of Condensed Matter, August 14–17, Albuquerque, New Mexico* (S.C. Schmidt, J.N. Johnson and L.W. Davison, Ed.). Elsevier Science Publishers, p. 117–120.

Johnson, J.N. and S.J. Green (1976) The mechanical response of porous media subject to static loads. In *The Effects of Voids on Material Deformation, 1976 Applied Mechanics Division Meeting, Salt Lake City, Utah, 14 June* (S.C. Cowin and M.M. Carroll, Ed.). American Society of Mechanical Engineers, p. 93–123.

King, H.H. and H.S. Janée (1987) Heating and stress release characterization of piezoresistive carbon gauges. Final Report to the Defense Nuclear Agency, Science Applications International Corp., Final Report SAIC-87/1656.

Krehl, P. (1978) Measurement of low shock pressures with piezoresistive carbon gauges. *Review of Scientific Instruments*, **49:** 1477–1484.

Krieg, R.D. (1978) A simple constitutive description for soils and crushable foams. Sandia National Laboratories, Report SC-DR-72-0883.

Larson, D.B. and G.D. Anderson (1979) Plane shock wave studies of porous geologic media. *Journal of Geophysical Research*, **84** (B9): 4592–4600.

Larson, D.B (1984) Shock-wave studies of ice under uniaxial strain conditions. *Journal of Glaciology*, **30** (105): 235–240.

Louie, N.A., W.W. Kinney and R.D. Reid, Jr. (1970) Dynamic properties of materials. US Air Force Weapons Laboratory, Report AFWL-TR-68-101.

Napadensky, H. (1964) Dynamic response of snow to high rates of loading. USA Cold Regions Research and Engineering Laboratory, Research Report 119.

Rice, M.H. (1980) PUFF74 EOS compilation. US Air Force Weapons Laboratory, Report AFWL-TR-80-21.

Sato, A. and R.L. Brown (1983) An evaluation of shock waves in unsaturated wet snow. *Annals of Glaciology*, **4:** 241–245.

Sato, A. (1987) Velocity of plastic waves in snow. In *Proceedings of the Davos Symposium on Avalanche Formation, Movement and Effects*. International Association of Hydrological Sciences, Publ. No. 162, p. 119–128.

Seaman, L.J. (1976) Lagrangian analysis for multiple stress or velocity gages in attenuating waves. *Journal of Applied Physics*, **45:** 4303–4314.

Swenson, D.V. and L.M. Taylor (1983) A finite element model for the analysis of tailored pulse stimulation of boreholes. *Journal for Numerical and Analytical Methods in Geomechanics*, **7**: 469–484.

Taylor, L.M. and D.P. Flanagan (1987) PRONTO 2D: A two-dimensional transient solid dynamics program. Sandia National Laboratories, Report Sand86-0594.

Vaughan, M.T. and S. Guggenheim (1986) Elasticity of muscovite and its relationship to crystal structure. *Journal of Geophysical Research*, **91** (B5): 4657–4664.

Wakahama, G. and A. Sato (1977) Propagation of a plastic wave in snow. *Journal of Glaciology*, **19**: 175–183.

APPENDIX A: Propagation of Stress Waves from the Lateral Edges of the Aluminum Buffer and Snow

Our PMMA flyer and target assembly was designed to have a relatively large diameter (about 200 mm) so that release waves generated at the lateral edge of the target would not arrive at the stress gauge locations until after the experiment ended. Stress histories recorded by the gauges in our experiment were sufficiently long that distortion of the uniaxial strain conditions by release waves before the experiment ended was likely. We examined the propagation of release waves from the edges of the target assembly into the center axis of the snow sample by constructing an axisymmetric 2D model of our experiment. The 2D model was about 260 mm in diameter, which corresponded to the diameter of the buffer plate (a radius of about 130 mm to the axis of symmetry), and had the same configuration on axis (with the exception that no gauges were embedded into the snow), material properties and dimensions as the 1D model (Fig. A1).

The main objective of conducting the 2D modeling was to develop a qualitative understanding of how release waves could distort the stresses in our shock impact experiment. In our discussion of the 2D modeling results we discussed pressure rather than the stresses parallel and perpendicular to the center axis of the sample since those stresses are about equal to each other and to the pressure.

The pressure distribution from the edge of the target to its center axis as a function of time for gauge plane 0 located in the aluminum buffer is shown in Figure A2a. Pressure distributions for the first snow element adjacent to the aluminum buffer and at the location of the gauge plane 1 in the snow are shown in Figures A2b and A2c. Figure A2a shows the four compressive pulses (also seen in the 1D model) associated with the initial impact of the PMMA flyer with the aluminum buffer and subsequent reflections from the aluminum/snow interface and PMMA/aluminum interface. The influence of the free edge of the aluminum buffer can be clearly seen as the stress pulses are reduced near the free edge and release waves move toward the center axis with time. The diagonally oriented trough in Figure A2a and the pressure ridge (A) are the result of the release wave propagating towards the center axis from the free surface with a propagation velocity of 4.0 ± 0.5 km s^{-1}. The release wave reaches the

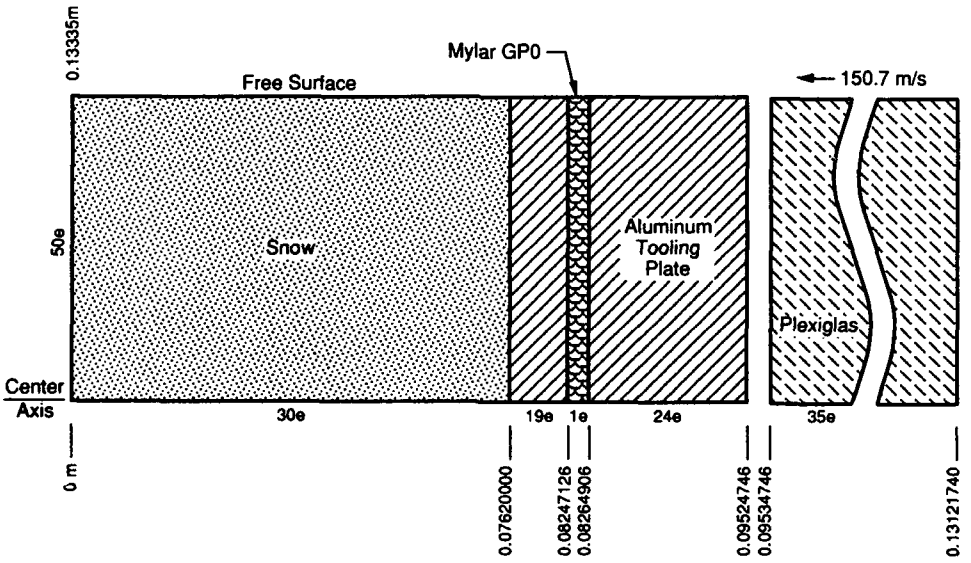

Figure A1. Schematic of the two-dimensional axisymmetric finite-element mesh for PRONTO 2D. Gauge plane 0 is designated by GP0 in the figure.

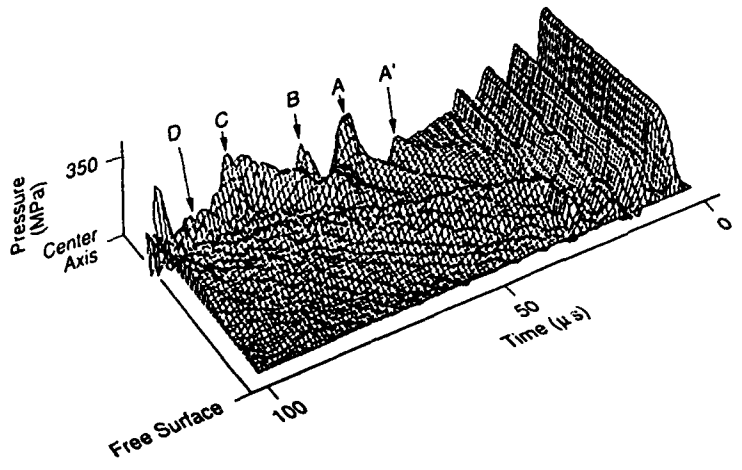

a. At gauge plane 0 in the aluminum.

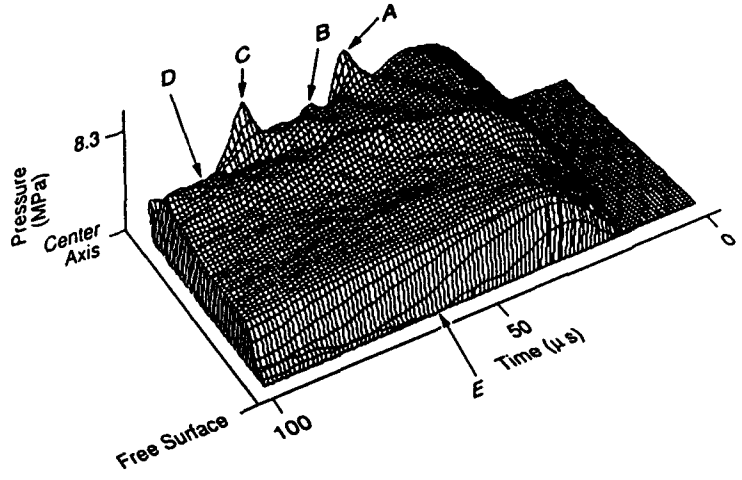

b. In the snow adjacent to the aluminum/snow interface.

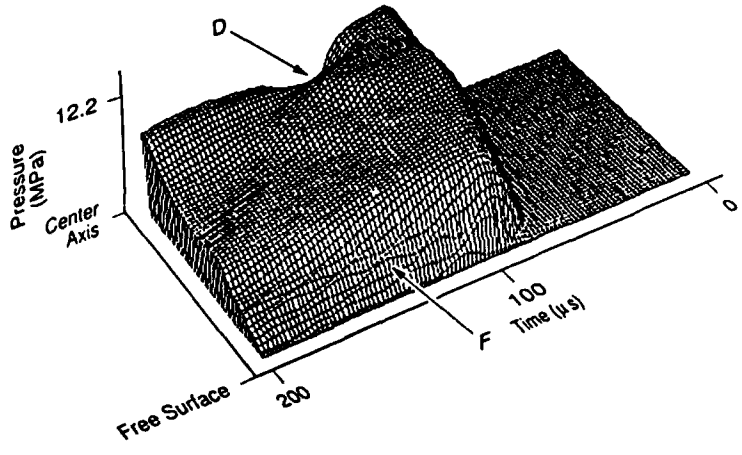

c. At the position of gauge plane 1 in the snow (A2c).

Figure A2. Pressure–time plots for three cross sections in the 2D axisymmetric model. Features A', A, B, C, D, E and F are discussed in the text.

center at approximately 46 μs. The pressure enhancement at the center axis (A) results from superposition of the corresponding release wave from the opposite side of the aluminum buffer. The several release waves seen in Figure A2a (A′, A, B, C) can be traced back to their origin at the free edge of the aluminum buffer and are associated with the four primary pressure pulses caused by the flyer's impact with the aluminum buffer.

Figure A2b shows that the release waves generated in the aluminum buffer are transmitted across the aluminum/snow interface. The pressure profile of the release waves in the snow is similar to that of the release waves in the aluminum buffer (see common features A, B, C and D in Fig. A2a and A2b). Release wave pressures are greatly attenuated when transmitted into the snow. The release wave generated at the lateral surface of the snow at feature E (Fig. A2b) is propagating inward at about 300 m s^{-1}. At this velocity the release wave does not reach the center axis until about 450 μs, well after the experiment has ended.

Figure A2c shows that the gross features from Figure A2b are still evident, such as the trough D; however, they are smoothed and attenuated considerably. The release wave generated at the snow's lateral edge F can also be seen propagating toward the center axis.

Our analysis indicates that release waves originating in the aluminum buffer arrive at the stress gauge planes embedded in the snow before the experiment ends. At gauge plane 1 the release waves arrive at about 96 μs and modulate the stress signal by about 1 MPa (the shock wave arrives at gauge plane 1 at 65 μs). The release waves begin modulating the shock wave front before it arrives at either gauge plane 2 or 3, with a maximum modulation of stresses of about 1 MPa. Release waves originating from the lateral edge of the snow sample do not affect the stresses at the gauge plane positions. The propagation time to the center axis for release waves generated at the snow's lateral edge is far longer than the duration of the experiment.

APPENDIX B: Modified Soil and Crushable Foams Model

Preliminary efforts to analyze our experimental measurements using the standard Soil and Crushable Foams model indicated that its unloading and reloading paths were too restrictive (Johnson et al. 1990). Geological materials exhibit nonlinearities when they are unloaded after shock wave passage (Johnson and Green 1976, Larson and Anderson 1979, Larson 1984). Additionally, porous materials can have a hysteresis when unloaded and then reloaded (Johnson and Green 1976). We modified the Soil and Crushable Foams model to include one or more linear or nonlinear unloading curves. Reloading can occur back along the unloading curve (no hysteresis) or along chords that connect the unloading curve to the $f_p(\varepsilon_v^{max})$, ε_v^{max} state. On loading, the P–V curve is defined by $f_p(\varepsilon_v^{max})$, as was the case for the original model.

Pressure is a function of volumetric strain and is given by

$$P = \begin{cases} f_p(\varepsilon_v^{max}) & \varepsilon_{v_t} = \varepsilon_v^{max} \\ f_{u_i}(\varepsilon_{v_t}) & \begin{array}{c} \varepsilon_{v_t} < \varepsilon_v^{max} \\ \varepsilon_{v_{u_{i-1}}} < \varepsilon_v^{max} \le \varepsilon_{v_{u_i}} \\ \varepsilon_{v_t} < \varepsilon_{v_{t-1}} \end{array} \quad i = 1, 2, 3, \ldots \\ f_{r_i}(\varepsilon_{v_t}) & \begin{array}{c} \varepsilon_{v_t} < \varepsilon_v^{max} \\ \varepsilon_{v_{u_{i-1}}} < \varepsilon_v^{max} \le \varepsilon_{v_{u_i}} \\ \varepsilon_{v_t} > \varepsilon_{v_{t-1}} \end{array} \end{cases} \tag{B1}$$

where ε_{v_t} is the volumetric strain at the current time step and $\varepsilon_{v_{t-1}}$ is the volumetric strain at the previous time step. The volumetric strain limits over which unloading $f_{u_i}(\varepsilon_{v_t})$ and reloading $f_{r_i}(\varepsilon_{v_t})$ functions are valid are given by $\varepsilon_{v_{u_i}}$ and $\varepsilon_{v_{u_{i-1}}}$ (Fig. B1).

For loading, the P–V curve is given by

$$f_p(\varepsilon_v^{max}) = S_n(\varepsilon_v^{max} - \varepsilon_{v_{n-1}}) + \sum_{k=0}^{n-1} S_k(\varepsilon_{v_k} - \varepsilon_{v_{k-1}}) \qquad n = 1,2,3,\ldots \tag{B2}$$

$$S_k = \begin{cases} 0 & k = 0 \\ \dfrac{P_k - P_{k-1}}{\varepsilon_{v_k} - \varepsilon_{v_{k-1}}} & k \ge 1 \end{cases}$$

where P_k and ε_{v_k} are specified pressure and volumetric strain values defining the P–V loading curve (Fig. B1) and the index n is determined by the condition that

$$\varepsilon_{v_{n-1}} < \varepsilon_{v_t} \le \varepsilon_{v_n}. \tag{B3}$$

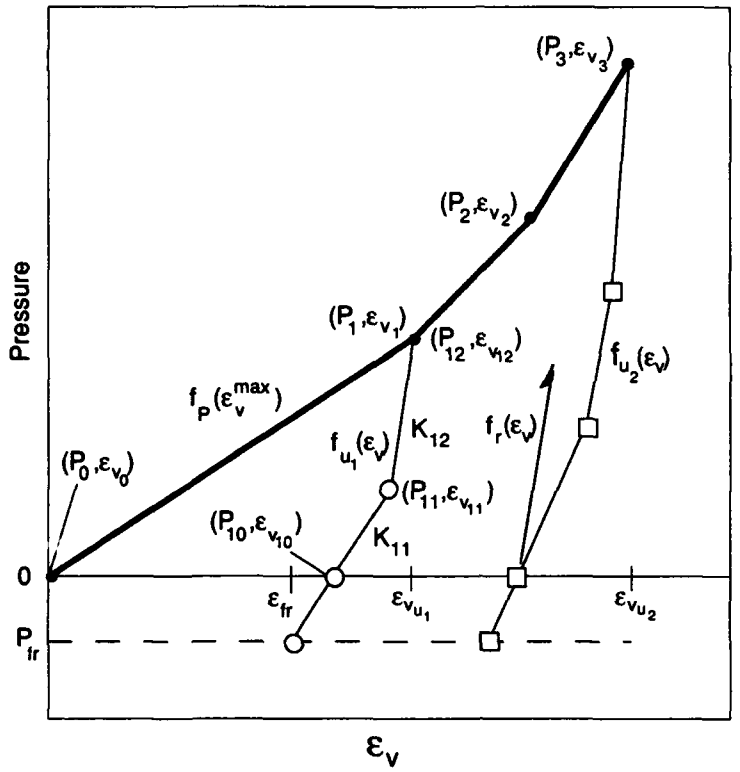

Figure B1. Pressure vs volumetric strain in terms of user-defined curves for pressure at the maximum volumetric strain $[f_P(\varepsilon_v^{max})]$, *pressure upon unloading* $[f_{u_i}(\varepsilon_{v_t})]$ *and pressure upon reloading* $[f_{r_i}(\varepsilon_{v_t})]$ *for the modified Soils and Crushable Foams material model.*

Tensile failure strain ε_{fr} is initially set to P_{fr}/K_0, where P_{fr} is the tensile failure pressure in the snow and K_0 is the snow's initial bulk modulus. Failure strain is recalculated for each increase in ε_v^{max} by unloading from $f_P(\varepsilon_v^{max})$ using $f_{u_i}(\varepsilon_{v_t})$.

Unloading *P–V* curves are defined by

$$f_{u_i}(\varepsilon_{v_t}) = K_{ij}\left(\varepsilon_{v_t} - \varepsilon_{ij-1}\right) + \sum_{m=0}^{j-1} K_{im}\left(\Delta\varepsilon_{im}\right) \qquad \begin{matrix} i = 1, 2, 3, \cdots \\ j = 1, 2, 3, \cdots \end{matrix} \tag{B4}$$

where

$$\varepsilon_{ij-1} = \varepsilon_{fr} - \frac{P_{fr}}{K_{il}} + \sum_{m=0}^{j-1} \Delta\varepsilon_{im} \tag{B5}$$

is the strain at the beginning of the curve segment containing ε_{v_t} and

$$\Delta\varepsilon_{im} = \begin{cases} 0 & m = 0 \\ \dfrac{P_{im} - P_{im-1}}{K_{im}} & m \geq 0 \end{cases} \tag{B6}$$

is the incremental strain across each curve segment in the unloading curve. The specified pressure P_{im} and slope K_{im} define the P–V unloading curve, where $K_{im} = 0$ when $m = 0$.

The index i specifies the unloading curve of interest and is determined by the condition that

$$\varepsilon_{v_{u_{i-1}}} < \varepsilon_v^{max} \leq \varepsilon_{v_{u_i}} . \tag{B7}$$

The index j specifies the curve segment over which a given modulus is defined (Fig. B1), where j is determined by the condition that

$$\varepsilon_{ij-1} < \varepsilon_{v_t} \leq \varepsilon_{ij} . \tag{B8}$$

Reloading can be in the reverse direction along the unloading curve, for which eq B3 applies and there is no hysteresis. Alternatively, reloading can be along chords connecting the unloading curve to the loading curve, producing a hysteretic unloading–reloading cycle. The slope of the reloading chord is required to be greater than or equal to the maximum slope of $f_P(\varepsilon_v^{max})$ between $\varepsilon_{v_{u_{i-1}}} < \varepsilon_v^{max} \leq \varepsilon_{v_{u_i}}$. Our analysis used reloading along chords where the reloading curve is given by

$$f_{r_i}(\varepsilon_{v_t}) = f_{r_i}(\varepsilon_{v_{t-1}}) + S\,\Delta\varepsilon_{v_t}$$

$$S = \frac{f_P(\varepsilon_v^{max}) - f_{r_i}(\varepsilon_{v_{t-1}})}{\varepsilon_v^{max} - \varepsilon_{v_{t-1}}} \tag{B9}$$

$$\Delta\varepsilon_{v_t} = \varepsilon_{v_t} - \varepsilon_{v_{t-1}} .$$

Figure 5 illustrates the loading, unloading and reloading curves used in this study, and Table 4 gives the values for P_k, ε_{v_k}, P_{im} and K_{im}.

*U.S. GOVERNMENT PRINTING OFFICE: 1992-600-063/60012

REPORT DOCUMENTATION PAGE

Form Approved
OMB No. 0704-0188

1. AGENCY USE ONLY (Leave blank)	2. REPORT DATE	3. REPORT TYPE AND DATES COVERED
	July 1992	

4. TITLE AND SUBTITLE
Shock Response of Snow:
Analysis of Experimental Methods and Constitutive Model Development

5. FUNDING NUMBERS
PR: 4A762784AT42
WU: CS/012

6. AUTHORS
Jerome B. Johnson, Jay A. Brown, Edward S. Gaffney,
George L. Blaisdell and Daniel J. Solie

7. PERFORMING ORGANIZATION NAME(S) AND ADDRESS(ES)
U.S. Army Cold Regions Research and Engineering Laboratory
72 Lyme Road
Hanover, N.H. 03755-1290

8. PERFORMING ORGANIZATION REPORT NUMBER
CRREL Report 92-12

9. SPONSORING/MONITORING AGENCY NAME(S) AND ADDRESS(ES)
Office of the Chief of Engineers
Washington, D.C. 20314-1000

10. SPONSORING/MONITORING AGENCY REPORT NUMBER

11. SUPPLEMENTARY NOTES

12a. DISTRIBUTION/AVAILABILITY STATEMENT
Approved for public release; distribution is unlimited.

Available from NTIS, Springfield, Virginia 22161.

12b. DISTRIBUTION CODE

13. ABSTRACT (*Maximum 200 words*)

A shock impact test was conducted on snow with an initial density of 400 kg m^{-3} using a large-diameter gas gun and Lagrangian stress gauges between layers of snow. The shock propagation velocity ranged from 240 to 207 m s^{-1}, the peak stresses in the snow were between 20 and 40 MPa, and the compacted snow density was less than 860 kg m^{-3}. Interpretation of the stress records was complicated by the unsteady nature of the shock, impedance mismatching between gauges and snow, multiply-reflected pulses, and release waves generated at the edge of the target. A dynamic finite-element analysis was used to interpret the data, to construct a constitutive relationship for the snow, and to examine the importance of the release waves. Model calculations indicate two release wave sources: the free edge of the target aluminum buffer and the edge of the snow in contact with the copper container. The aluminum buffer release waves contain both shear and dilatational components. Transmission across the aluminum/snow interface significantly attenuated dilatational waves and essentially eliminated the shear waves. The snow/copper release wave did not arrive at the stress gauge position until after the end of the experiment.

With the aid of model calculations, the pressure volumetric–strain (P–V) curve for initial shock loading was determined from arrival time information and stress measurements at the embedded gauges. Stress signals caused by reflected waves were used to determine the reloading and unloading P–V curve. The P–V response for shock loading was found to be much stiffer than that for quasi-static loading. The unloading P–V curves used in model calculations were nonlinear functions of volumetric strain with linear reloading.

14. SUBJECT TERMS
Shock impact tests
Snow

15. NUMBER OF PAGES
23

16. PRICE CODE

17. SECURITY CLASSIFICATION OF REPORT	18. SECURITY CLASSIFICATION OF THIS PAGE	19. SECURITY CLASSIFICATION OF ABSTRACT	20. LIMITATION OF ABSTRACT
UNCLASSIFIED	UNCLASSIFIED	UNCLASSIFIED	UL